A Compliant and Precise Pneumatic Rotary Drive Using Pneumatic Artificial Muscles in a Swash Plate Design

Johannes T. Stoll [1], Kevin Schanz [1] and Andreas Pott [2]

***Abstract*— Compliant and precise rotary drive units are essential for the design of articulated robots that are capable of safe human-robot collaboration. In this paper, we present a new pneumatic rotary drive unit that combines the compliance of pneumatic systems with the ability to perform high precision positioning. We use pneumatic artificial muscles (PAMs) pulling on a swash plate to avoid the stick-slip phenomenon and to realize adjustable stiffness. Furthermore, the presented drive unit can operate in 360° continuous rotation. These properties make the drive particularly suitable for the later use in human-robot collaboration. We explain the mechanic design as well as the pneumatic and electric control system that we use to operate the drive unit. We derive the equations to calculate the static torque distribution and compare the theoretical results to the data measured on the realized laboratory test stand, depicted in figure 1. The accuracy of the used 16-bit encoder is achieved and adjustable stiffness is realized and measured on the laboratory test stand. The measurements of the reaction to a step response are discussed based on a first and basic control strategy.**

I. Introduction

Today's compliant articulated robots, suitable for the use in human-robot collaboration, make use of the well-known, state-of-the-art drive units, electric motors with attached high ratio gearboxes. Conventional articulated robots consist of multiple of these intrinsically stiff and not back-drivable rotary drive units. Hence, these systems are not safe by design. One way to achieve compliant behavior with these drive units is to use additional torque sensors and to implement high end control algorithms. Drive units and robotic systems with integrated torque sensors are presented in [1], [2]. To add an elastic element in series to the stiff drive unit also results in a compliant drive unit. Therefore, this type is called series elastic actuator, [3], [4]. Another way to enable safe human-robot collaboration is to add sensing robot skins to the robot. These skins use either distance or tactile sensing to ensure safe human-robot collaboration. All the above-mentioned approaches use additional and often high-end components, leading to higher error rates and to increased prices for the final robot system.

In contrary to the described stiff and precise electric drive units, pneumatically actuated drive units are intrinsically compliant due to the natural compressibility of the air which is used to actuate those systems. Precise positioning with pneumatic drive units known from conventional automation is very hard to realize since these systems suffer from the stick-slip phenomenon. Soft robots investigated in research are described in [5], [6]. Many of these robots use inflatable and therefore soft but inaccurate structures making precise positioning, as needed in most industrial robot applications, very hard. Precise positioning and compliance are the most important specifications required in human-robot collaboration. The motivation of the present work is to create a new pneumatic rotary drive unit that meets these specifications.

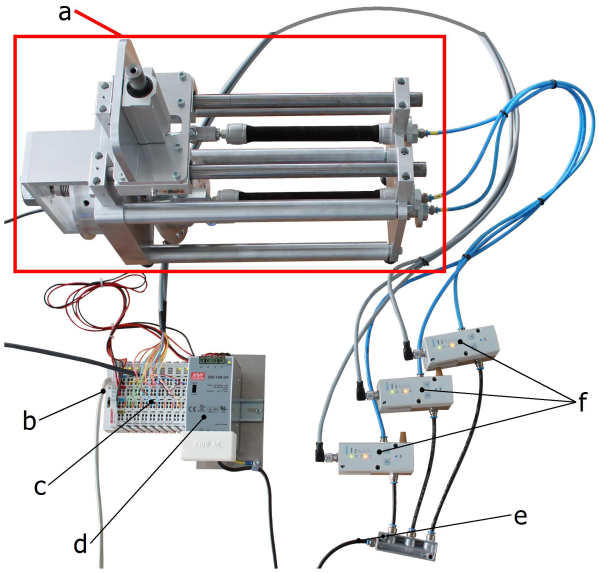

Fig. 1. Overview of the laboratory test stand, drive unit a, Ethernet connection b, PLC control c, power supply d, air supply e, proportional valves f

Research on compliant pneumatic drive units for the use in robotics usually investigates antagonistic pairs of identical working chambers. Antagonistic pairs of rolling diaphragm cylinders are investigated at Disney research [7] and a robot is realized using them [8]. Antagonistic gaiter pairs are investigated at Friedrich-Wilhelm-Bessel-Institut, explaining the design and the mechanical properties [9] as well as the control of these systems [10]. At the Karlsruhe Institute of Technology, fiber reinforced, double layer, bellows are designed and used in an antagonistic configuration to create actuated robotic joint elements [11], [12]. An overview on multiple pneumatic joint designs is given in section two of [12]. A survey on different applications of pneumatic

*This work was not supported by any organization.

[1]Johannes T. Stoll and Kevin Schanz are with the department "Robot and Assistive Systems" at the Fraunhofer Institute for Manufacturing Engineering and Automation IPA, 70569 Stuttgart, Germany
johannes.stoll@ipa.fraunhofer.de

[2]Andreas Pott is with the Institute for Control Engineering of Machine Tools and Manufacturing Units (ISW), University of Stuttgart, 70174 Stuttgart, Germany
andreas.pott@isw.uni-stuttgart.de

artificial muscles (PAM) is given in [13]. Many different researchers deal with the modeling, simulation, and control of PAMs in antagonistic setups and with drive units and robot arms that comprise antagonistic pairs of PAMs, [14–18].

In a pending patent [19], different drive configurations using either bellow actuators or PAM actuators as working chambers are presented. A drive unit comprising three bellow actuators is realized and investigated in [20]. The operating principle is proved and basic measurements are performed. Unfortunately, the prototype bellow elements cannot withstand pressure levels above 400 kPa and they are not durable enough to investigate control strategies that are necessary to control the drive unit.

II. Approach

A lubricated sliding seal is used in standard pneumatic drives like cylinders to seal the working chamber against the surrounding environment. The static friction coefficient μ_s between this seal and the cylinder wall is clearly higher than the kinetic friction coefficient μ_k between them. Hence, the static friction is higher than the kinetic friction force, $F_s \gg F_k$. This finally leads to the well-known stick-slip phenomenon [21], which makes precise positioning very difficult. Hence, we propose to use inflatable working chambers with flexible walls and variable volume to avoid the stick-slip phenomenon by design. In this approach, we use PAMs as working chambers. These PAMs are state-of-the-art industry products and are thus durable and easy to procure. A PAM contracts along his longitudinal axis when it is filled with compressed air and it exerts a pulling force.

A. Operating principle

We designed a swash plate arrangement to convert the linear contracting motion of the PAMs into a rotary motion of the drive shaft. Figure 2 depicts a schematic of the swash plate design with only one pulling force exerted onto the the outer swash plate. The outer swash plate is pivoted around the drive shaft and does not rotate. It only changes the orientation of the fixed inclination β of the swash plate depending on the angular position φ of the drive shaft. A rotatory motion of the outer swash plate is prevented by an additional fixture, not shown in the schematic, but depicted in figure 3 as g. Hence, the pulling force exerted from a muscle onto the outer swash plate leads to a change in the orientation of the inclination β and therefore leads to a rotation of the drive shaft.

III. Theory

The calculation of the total torque, generated by the forces exerted from the muscles onto the outer swash plate, is derived by using the geometric relations depicted in figure 2.

It is clear, that the current torque M is a function

$$M = f(\varphi, F_{mus,i}, \beta, n) \tag{1}$$

dependent on the current position φ, and the forces $F_{mus,i}$ exerted onto the outer swash plate by the n muscles. The

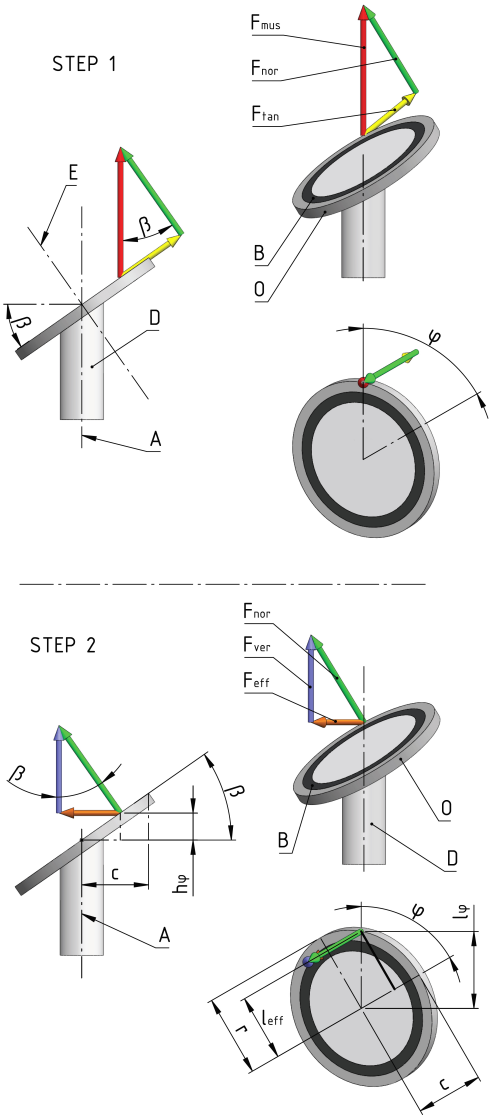

Fig. 2. Schematic representation of the operating principle and the force components, drive shaft with inner swash plate D, four point bearing B, outer swash plate O, angular position φ, inclination of the swash plate β, rotary axis A of the drive shaft, rotary axis of the outer swash plate E. Step one: force of the PAM F_{mus}, normal force of the PAM F_{nor}, tangential force of the PAM F_{tan}, step two: vertical force component of F_{nor}: F_{ver}, horizontal force component of F_{nor}: F_{eff}, radius of the point of attack of F_{mus} and semi-major axis of the projected ellipse r, current projected radius l_φ, effective lever arm l_{eff}, semi-minor axis c of the projected ellipse, current height h_φ

argument β describes the inclination angle of the swash plate. As a result of the construction, the total torque is the sum of the torques, generated by all muscles. The torque on the drive shaft M_i generated by the muscle i is calculated by

$$M_i = F_{eff,i}\, l_{eff,i} \tag{2}$$

with $F_{eff,i}$ being the effective force of the muscle and $l_{eff,i}$ the effective lever arm.

The force exerted onto the outer swash plate by one working chamber is split up in two steps, to finally calculate the static torque generated by that PAM. In step one of the schematic, see figure 2, the force exerted from the muscle $F_{mus,i}$ is split

up into the normal force $F_{nor,i}$ and the tangential force $F_{tan,i}$. The tangential force component is absorbed by the additional fixture not shown in the schematic but depicted in figure 3 as g. Only the normal component of the muscle force

$$F_{nor,i} = F_{mus,i}\cos(\beta) \tag{3}$$

is transmitted by the four point bearing towards the inner swash plate and the drive shaft. In step two of the schematic, see figure 2, the remaining force $F_{nor,i}$ is again split up into a vertical component $F_{ver,i}$ and a horizontal component $F_{eff,i}$. $F_{ver,i}$ is absorbed by the structure while

$$F_{eff,i} = -F_{nor,i}\sin(\beta) \tag{4}$$

generates a torque around the rotary axis. Together with equation (3), the effective force $F_{eff,i}$ is calculated by

$$F_{eff,i} = -F_{mus,i}\sin(\beta)\cos(\beta), \tag{5}$$

which can be simplified to

$$F_{eff,i} = -\frac{1}{2}F_{mus,i}\sin(2\beta). \tag{6}$$

The effective lever l_{eff} depends on the current position φ_i, which takes the offset of the muscle into account, the inclination angle β and the radius r to the point of attack of $F_{eff,i}$, which produces

$$l_{eff,i} = f(\varphi_i, \beta, r). \tag{7}$$

To derive the exact length of $l_{eff,i}$, the distance perpendicular to the effective force in the horizontal plane has to be determined. The rotary axis of the drive shaft A is perpendicular to the horizontal plane. The straight connection between the rotation axis A and the point of attack of $F_{eff,i}$ is r independent of the current position φ_i. This holds true, because r is the radius of the point of attack of $F_{mus,i}$ to the rotary axis E of the outer swash plate. This plane is inclined by the angle β. The two axes A and E intersect in the inclined plane. Since l_{eff} has to be perpendicular to the rotation axis A, the circle of the points of attack of the forces $F_{mus,i}$ with the radius r is projected from the inclined plane onto the horizontal plane, resulting in an ellipse. The distance l_φ depends on the position φ and the shape of the ellipse. The semi-major axis of the ellipse is identical with the distance r. The semi-minor axis c is determined by the projection

$$c = r\cos(\beta), \tag{8}$$

which transforms the radius r to the plane, perpendicular to the rotation axis of the drive shaft A. Together with the formula for an ellipse in polar coordinates

$$l_\varphi = \frac{cr}{\sqrt{r^2\cos^2(\varphi) + c^2\sin^2(\varphi)}} \tag{9}$$

with the semi-minor axis c and semi-major axis r, this results in the distance l_φ from the rotation axis to the projection of the suspension point of the muscle. By projecting l_φ onto the direction perpendicular to the direction of F_{eff} in the plane perpendicular to the rotation axis, the equation

$$l_{eff,i}(\varphi_i) = l_{\varphi_i}\sin(\varphi_i) \tag{10}$$

for the effective lever l_{eff} is determined. The position φ_i describes the current position of the drive shaft with respect to the muscle i with a simple phase offset

$$\varphi_i = \varphi - \frac{2\pi}{n}(i-1), \tag{11}$$

with n being the number of muscles.
The total torque at the shaft therefore results in

$$M = \sum_{i=1}^{n} -\frac{1}{2}F_{mus,i}\sin(2\beta)\frac{cr}{\sqrt{r^2\cos^2(\varphi_i) + c^2\sin^2(\varphi_i)}}\sin(\varphi_i), \tag{12}$$

representing the sum of all torques.

IV. Laboratory Test Stand

A. Mechanical Design

The intention of the present mechanical design is to create a solid laboratory test stand that proves the operating principle and allows accurate measurements. In figure 3, a sectional of the CAD-model of the realized laboratory test stand is depicted. The structure and all other fixed and not moving parts like the encoder are tinted brown. All green tinted parts are connected to the drive shaft and pivoted by the shaft bearings, these parts rotate together with the drive shaft around the main axis of rotation. The outer swash plate and the parts connected to it are tinted pink. A rotation of these parts is prevented by the additional fixture tinted in cyan. The outer swash plate is pivoted with a four point bearing around the inner swash plate and the drive shaft. The PAMs are tinted blue. The encoder is a Sick DFS60AS4PC65536, it has a resolution of 16 bit. Hence, 65536 steps are equally distributed over 360°, finally resulting in an accuracy of 0.0055° per encoder step. The test stand is designed modularly to allow the investigation of different configurations. As a result, three to five PAMs can be attached to the swash plate and drive shafts with different inclination angles can be installed. Throughout this work, we use PAMs with a nominal length of 200 mm and a nominal diameter of 20 mm as working chambers (FESTO, DMSP-20-200N-AM-CM). The radius r is set to 75 mm throughout this work.

B. Pneumatic Setup and Electronic Control

Proportional valves (FESTO, VPPM-6L-L-1-G18-0L6H-V1P-S1) are used to set the air pressure in the PAMs to the desired level. In figure 4, the pneumatic control scheme is depicted, each PAM is individually controlled by the associated proportional valve. To realize different control strategies, a computer is connected to a modular Beckhoff PLC. The PLC consists of the EtherCAT coupler EK1101, three analog output interfaces EL4002, three analog input interfaces EL3162 and one incremental encoder interface EL5101-0010.

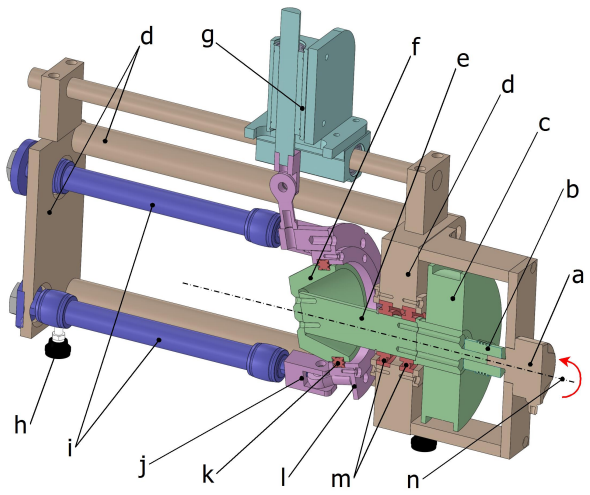

Fig. 3. Sectional view of the 3D-CAD model with three PAMs, encoder a, coupling b, cable drum c, structure d, drive shaft e, inner swash plate f, additional fixture g, leveling foot h, PAMs i, connecting elements j, four point bearing k, outer swash plate l, shaft bearings m, centerline of the rotary axis n, red arrow indicating the positive direction of rotation and φ

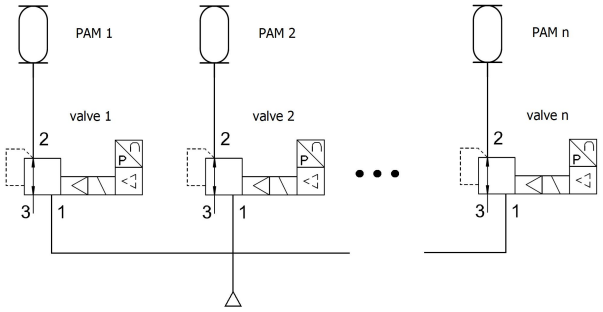

Fig. 4. Pneumatic control scheme of the laboratory test stand. Drive configurations with $n = 3$, $n = 4$ and $n = 5$ valves and PAMs can be investigated.

V. Results

In figure 5, the realized laboratory test stand is depicted. Three to five PAMs are used in the modular setup, figure 5 depicts the configuration with 5 PAMs. Moreover, the drive shaft with the fixed inclination β can be changed. Within the present work, inclinations of $\beta = 8°, 10°, 12°$ are investigated. At the end of the drive shaft, the encoder is connected with a coupling. The cable drum is mounted on the drive shaft, see h in figure 5. Weights can be attached to the cable to deliver a constant external torque to the drive shaft, independent of the current angular position φ.

A. Static Torque Distribution

The static torque generated by the pulling forces of the muscles is measured on the laboratory test stand. To measure the torque, a lever arm is attached to the drive shaft instead of the cable drum. An additional plate with suitable threads allows to mount a load cell between the lever arm and the plate in steps of 15°. Hence, we present the static torque distribution measured at 24 discrete positions. The load cell is a Micro Load Cell CZL635 from Phidgets, it

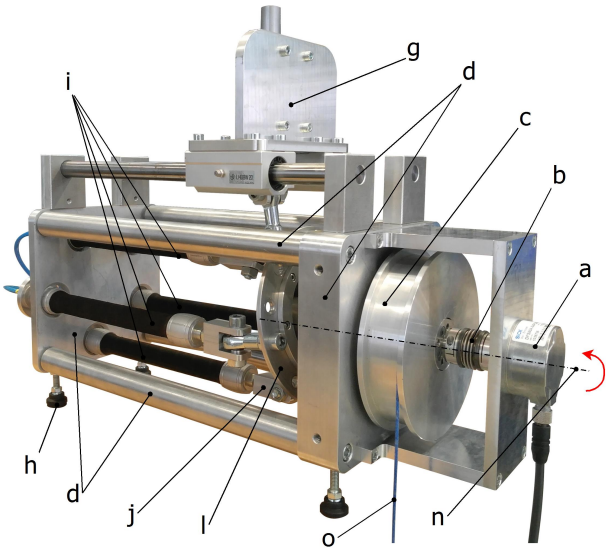

Fig. 5. Realized modular laboratory test stand with five PAMs, see figure 3 for the description of the letters a to n, cable to attach load o

measures weights up to 20 kg. The load cell is connected to the PhidgetBridge 4-Input board, which is linked by USB to a computer. The desired pressure level is set by the proportional valve and applied to the PAM. Afterwards, the force at the end of the lever arm is measured with the load cell. Figure 6 depicts how changes in the pressure level applied to working chamber number one affect the generated torque. The relation between the applied pressure level and torque as well as the relation between the inclination and torque is quite linear within the investigated range. Increasing the inclination of the swash plate leads to higher maximum torques but also increases the variation of the torque generated, see figure 6. We measure the torque generated by each PAM individually. Hence, the total torque is calculated as a sum of the individual torques. This has the advantage, that we use the same load cell for all presented measurements, which reduces the influence of calibration errors and differences between load cells of different ranges. In total, 27 measurement series regarding the static torque distribution are conducted with different configurations of the drive unit. The inclination β is varied with discrete values of 8°, 10° and 12°. The number of PAMs n is varied from 3 to 5 and pressure levels of 400, 500 and 600 kPa are applied to the PAMs.

In figure 7, the measured total static torque distribution is depicted for a configuration comprising five PAMs, with the inclination $\beta = 12°$, while the pressure level is set to $p = 600$ kPa and compared to the calculated static torque distribution. Increasing the amount of working chambers in the drive unit results in a higher and more equally distributed total torque. Unfortunately, the use of more working chambers increases the needed amount of proportional valves since every PAM has to be controlled individually. The comparison between calculated and measured torque is made possible through the equations in chapter III, combined with

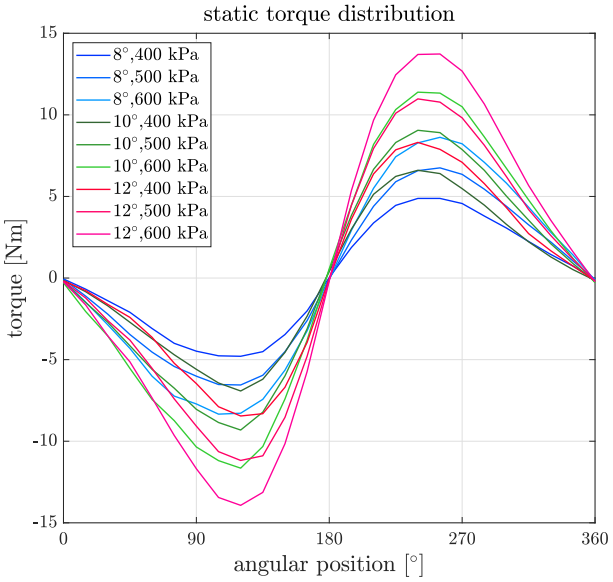

Fig. 6. Measured static torque distribution for PAM 1 at different pressure levels p and different inclinations β

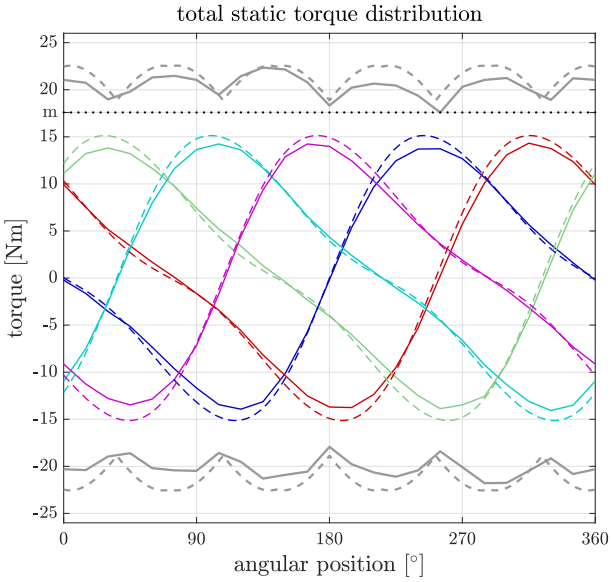

Fig. 7. Measured and calculated values for the configuration with five PAMs, $\beta = 12°$ and $p = 600$ kPa. Measured values are represented with continuous lines, calculated values are represented by dashed lines, the static torque distribution for each PAM is colored: blue for PAM 1, red for PAM 2, pink for PAM 3, green for PAM 4 and cyan for PAM 5. The total static torque distribution is depicted grey, m depicts the maximum continuous torque possible

values given by the software Muscle Sim from FESTO. Specifying contraction and applied pressure, the software returns simulated force values for the PAM of the type MAS. This PAM is very similar to the PAM of the type DMSP used throughout the present work, leading to the results depicted by the dashed lines in figure 7. The maximum possible continuous torque output on the drive shaft is depicted with the black dotted line in figure 7 and the value is found to be $m = 17.6$ Nm for the presented configuration.

B. Adjustable Stiffness

The measurements regarding the adjustable stiffness are again conducted with the configuration of five PAMs and an inclination of $\beta = 12°$. The two working chambers number one and two are inflated with the chosen pressure level and the drive shaft is manually positioned in the beginning of a measurement series. Now different weights are attached to the cable which is wound up on the cable drum. We start with a weight of 1 kg, resulting in an external torque of 0.74 Nm and measure the deflection of the angular position φ. Afterwards we increase the weight and again measure the deflection. Four measurement series are conducted, inflating the PAMs with 300, 400, 500, and 600 kPa. Weights of 1, 2, 3, 5, 6, 7 and 8 kg are connected to the cable during a measurement series. The internal controllers of the proportional valves are active during the measurements. As a result, the pressure in the working chambers is kept constant even after the deflection. The measurement data depicted in figure 8 shows a linear relation between deflection and applied external torque. Increasing the pressure level in the PAMs leads to higher stiffness of the drive unit.

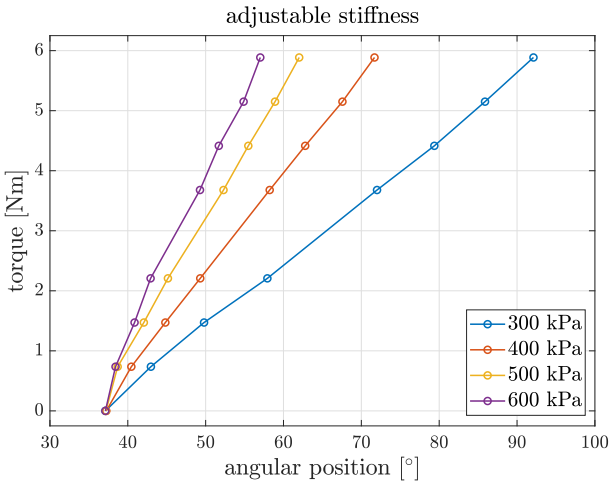

Fig. 8. Deflecting the angular position with different external torques applied, starting at the same angular position, constant pressure levels applied to PAM 1 and PAM 2, $\beta = 12°$, $n = 5$

C. High Precision Positioning

The capability to perform high precision positioning is mandatory if the drive unit is supposed to be used in robotics. The Sick 16-bit encoder detects the angular position with an accuracy of 0.0055°. The proportional valves can be operated between 6 and 600 kPa and receive input signals from $0 - 10$ V. In figure 9, the angular position is depicted in relation to the smallest possible incremental steps for pressure values detected on the input of the control. To evaluate the possibility of reaching every incremental step of the angular position encoder, PAM one is inflated to 400 kPa, PAM two to 300 kPa and PAM three to 200 kPa. Then the pressure value in PAM three is increased by 0.000183 kPa every 10 ms. This is the smallest amount of pressure that can be added within the resolution of the PLC. Following

these steps, it is shown that in the depicted section the pressure has to increase by one or more increments before the angular position increases one increment. Hence, we do not encounter any issues during our investigations that are caused by the occurrence of stick-slip phenomena. As a result, it is possible to position the drive at any desired set point position within the 360° detectable with the encoder.

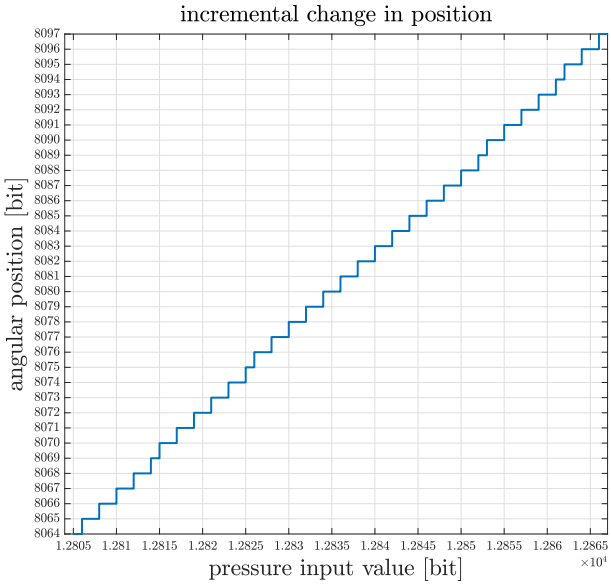

Fig. 9. Increasing pressure p in PAM 3 as slow as possible in relation to the change of the angular position φ in a section with ideal characteristics

D. Reaction to a Step Response

Positioning should be possible in a short amount of time in robotics. Hence, a basic control strategy is implemented to make quick positioning possible, with minimal offset to the set point position. To show that the drive can be used in such a manner, a PID-controller with state-feedback is implemented. The different states are the current position φ, the angular velocity $\dot{\varphi} = \omega$ and the integrated difference between wanted position and current position $\xi = \int (w - x) \mathrm{d}t$. As a result of the current design, only φ can be measured. While ξ can be calculated, ω has to be determined via an observer, which is directly implemented in the PLC.
Adding a prefilter to the controller results in the ability to rotate the drive shaft into any desired position, with slightly overshooting the targeted position. Figure 10 shows the system response to a step input with three different muscle setups. It can be seen, that all configurations reach the desired set-value within a few seconds and with marginal overshoot of less than 0.35%. The implementation with five muscles results in the smoothest movement. Further investigation of different control approaches will be part of future research.

VI. Conclusions and Future Work

We have presented a rotary drive design consisting of three to five PAMs that exert pulling forces onto a swash plate. We derive the equations to calculate the static torque generated by the pulling force of the muscles. The static

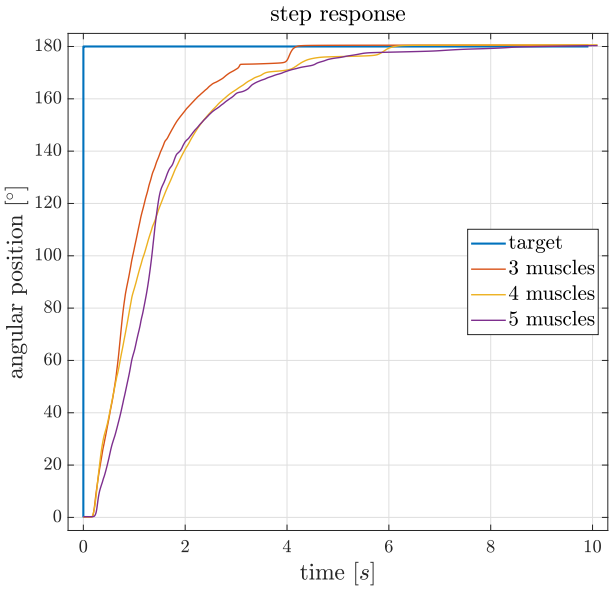

Fig. 10. Comparison of step responses of the controller, drive unit configurations with three, four and five PAMs, starting position 0°, set point position 180°, inclination $\beta = 12°$

torque distribution is measured on the laboratory test stand and compared to the calculated data. The obtained data sets match well regarding the characteristics of the static torque distribution. A maximum constant torque of 17.6 Nm is achieved when five PAMs are used in combination with the maximum inclination angle, $\beta = 12°$, while the maximum pressure level of $p = 600$ kPa is applied. The variation of the torque for this configuration is 27% in relation to the maximum constant torque stated above. The drive unit avoids the stick-slip phenomenon by design and is therefore capable of performing high precision positioning, reaching the accuracy of the used 16-bit encoder, 0.0055°. Compliance is realized and adjustable stiffness has been confirmed with measurement data. We present the step response for three different configurations of the drive unit to reach the desired set-value within 10 seconds.
The theoretical description regarding the force $F_{mus,i}$ exerted by a PAM onto the outer swash plate can be improved. A task in future work could be to characterize the PAMs regarding their relation between generated force, current contraction, and applied pressure level. Moreover, new modeling approaches regarding these relations for PAMs of the FESTO DMSP type are presented in [22] and can be implemented to improve the accuracy of the calculated static torque distribution. Investigating different control approaches known from electric motors as well as the evaluation of these approaches on the laboratory test stand could be a part of future work. The presented drive unit is relatively voluminous and heavy, since it is designed to prove the operating principle and to allow accurate measurements. Hence, a mechanical redesign could be part of future work, seeking to realize a compact and lightweight drive unit.

REFERENCES

[1] A. Albu-Schäffer, S. Haddadin, C. Ott, A. Stemmer, T. Wimböck, and G. Hirzinger, "The dlr lightweight robot: design and control concepts for robots in human environments," *Industrial Robot: an international journal*, vol. 34, no. 5, pp. 376–385, Aug. 2007.

[2] S. Rader, L. Kaul, P. Weiner, and T. Asfour, "Highly integrated sensor-actuator-controller units for modular robot design," in *2017 IEEE International Conference on Advanced Intelligent Mechatronics (AIM)*. IEEE, Jul. 2017, pp. 1160–1166.

[3] G. A. Pratt and M. M. Williamson, "Series elastic actuators," in *Proceedings 1995 IEEE/RSJ International Conference on Intelligent Robots and Systems. Human Robot Interaction and Cooperative Robots*, vol. 1, Aug. 1995, pp. 399–406.

[4] F. Negrello, M. Garabini, M. G. Catalano, J. Malzahn, D. G. Caldwell, A. Bicchi, and N. G. Tsagarakis, "A modular compliant actuator for emerging high performance and fall-resilient humanoids," in *2015 IEEE-RAS 15th International Conference on Humanoid Robots (Humanoids)*, Nov. 2015, pp. 414–420.

[5] A. Verl, A. Albu-Schffer, O. Brock, and A. Raatz, *Soft Robotics: Transferring Theory to Application*. Springer, Berlin, 2015.

[6] D. Rus and M. T. Tolley, "Design, fabrication and control of soft robots," *Nature*, vol. 521, no. 7553, pp. 467–475, May 2015.

[7] J. P. Whitney, M. F. Glisson, E. L. Brockmeyer, and J. K. Hodgins, "A low-friction passive fluid transmission and fluid-tendon soft actuator," in *2014 IEEE/RSJ International Conference on Intelligent Robots and Systems*, Sep. 2014, pp. 2801–2808.

[8] J. P. Whitney, T. Chen, J. Mars, and J. K. Hodgins, "A hybrid hydrostatic transmission and human-safe haptic telepresence robot," in *2016 IEEE International Conference on Robotics and Automation (ICRA)*, May 2016, pp. 690–695.

[9] O. Ivlev, "Modular multi-sensory fluidic actuator with pleated rotary elastic chambers," in *IFAC Proceedings*, vol. 39, no. 16, Sep. 2006, pp. 271–276.

[10] M. Mihajlov, M. Hubner, O. Ivlev, and A. Graser, "Modeling and control of fluidic robotic joints with natural compliance," in *2006 IEEE International Conference on Control Applications*, Oct. 2006, pp. 2498–2503.

[11] I. Gaiser, S. Schulz, H. Breitwieser, and G. Bretthauer, "Enhanced flexible fluidic actuators for biologically inspired lightweight robots with inherent compliance," in *2010 IEEE International Conference on Robotics and Biomimetics*, Dec. 2010, pp. 1423–1428.

[12] I. Gaiser, R. Wiegand, O. Ivlev, A. Andres, H. Breitwieser, S. Schulz, and G. Bretthauer, *Compliant robotics and automation with flexible fluidic actuators and inflatable structures*. Rijeka: IntechOpen, Oct. 2012, ch. 22. [Online]. Available: https://doi.org/10.5772/51866

[13] G. Andrikopoulos, G. Nikolakopoulos, and S. Manesis, "A survey on applications of pneumatic artificial muscles," in *2011 19th Mediterranean Conference on Control Automation (MED)*, Jun. 2011, pp. 1439–1446.

[14] Z. Situm and S. Herceg, "Design and control of a manipulator arm driven by pneumatic muscle actuators," in *2008 16th Mediterranean Conference on Control and Automation*, Jun. 2008, pp. 926–931.

[15] G. Tonietti and A. Bicchi, "Adaptive simultaneous position and stiffness control for a soft robot arm," in *IEEE/RSJ International Conference on Intelligent Robots and Systems*, vol. 2, Sep. 2002, pp. 1992–1997.

[16] B. Tondu, "A seven-degrees-of-freedom robot-arm driven by pneumatic artificial muscles for humanoid robots," *The International Journal of Robotics Research*, vol. 24, pp. 257–274, Apr. 2005.

[17] B. Tondu and P. Lopez, "Modeling and control of mckibben artificial muscle robot actuators," *IEEE Control Systems Magazine*, vol. 20, no. 2, pp. 15–38, Apr. 2000.

[18] M. Martens, A. Passon, and I. Boblan, "A sensor-less approach of a torque controller for pneumatic muscle actuator driven joints," in *2017 3rd International Conference on Control, Automation and Robotics (ICCAR)*, Apr. 2017, pp. 477–482.

[19] J. T. Stoll, "Drehantrieb," german Patent DE 10 2016 217 198 A1, Sep. 09, 2018.

[20] J. T. Stoll and A. Pott, "A compliant, high precision, pneumatic rotary drive for robotics," in *International Symposium on Robotics*. VDE VERLAG GMBH, Berlin, Offenbach, Jun. 2018, pp. 1–7.

[21] C. Canudas de Wit, H. Olsson, K. J. Astrom, and P. Lischinsky, "A new model for control of systems with friction," *IEEE Transactions on Automatic Control*, vol. 40, no. 3, pp. 419–425, Mar. 1995.

[22] M. Martens and I. Boblan, "Modeling the static force of a festo pneumatic muscle actuator: A new approach and a comparison to existing models," *Actuators*, vol. 6, no. 4, Nov. 2017. [Online]. Available: http://www.mdpi.com/2076-0825/6/4/33